J. Space Weather Space Clim., **5**, A28 (2015)
DOI: 10.1051/swsc/2015029

RESEARCH ARTICLE OPEN ACCESS

Cancellation analysis of current density in solar active region NOAA10019

Gaetano De Vita[1,2], Antonio Vecchio[3], Luca Sorriso-Valvo[1,*], Carine Briand[4], Leonardo Primavera[2], Sergio Servidio[2], Fabio Lepreti[2], and Vincenzo Carbone[2]

[1] CNR-Nanotec, UOS di Cosenza, ponte P. Bucci, cubo 31C, 87036 Rende, Italy
[*]Corresponding author: lucasorriso@gmail.com
[2] Dipartimento di Fisica, Università della Calabria, ponte P. Bucci, cubo 31C, 87036 Rende, Italy
[3] INGV – sede di Cosenza, ponte P. Bucci, cubo 30C, 87036 Rende, Italy
[4] LESIA – Observatoire de Paris, 5 place Jules Janssen, 92195 Meudon, France

Received 15 December 2014 / Accepted 24 July 2015

ABSTRACT

Solar flares are often associated with changes in the fine magnetic structure of the emitting active region. Such topological modification results in variations of both the scaling properties of the fields' fluctuations, and the fractal dimension of the associated gradients. The use of cancellation analysis of the current density has been attempted for the identification and quantitative estimation of such changes. The characteristics of the magnetic vector as measured by THEMIS telescope for the active region NOAA10019 have been studied in this paper, suggesting the presence of disrupted current filaments. The variation of the fractal dimension of the current structures, and in particular their smoothing, is discussed in relationship with occurrence of one flare in the active region.

Key words. Active Regions – Solar flares – Photosphere

1. Introduction

Solar magnetism is characterized by the complex dynamo processes occurring in the Sun. Consequently, emergence of dynamic magnetic field from the solar interior within a convectively driven plasma flow originates a number of transient phenomena. At the photospheric level, one of the most evident aspects of magnetic activity is the generation of active regions (ARs), which are regions of more or less extended and concentrated emerging magnetic field. Active regions appear at the photospheric level as bi- or multipolar magnetic structures, which may include the presence of pores and sunspots, one of the most striking phenomena of solar magnetism. Active regions are often associated with eruptive phenomena, such as flares, which in turn may have consequences on the Earth-space environment, therefore being of great strategic importance for space weather. One of the main goals in solar physics is the identification of magnetic signature of the occurrence of flares within ARs. In recent years, cancellation analysis has been used to correlate the topology of solar magnetic fields in active regions to the occurrence of flares (Abramenko et al. 1998; Yurchyshyn et al. 2000, 2012; Sorriso-Valvo et al. 2004, 2015). Such analysis is complicated by the scarce availability of photospheric magnetic vector measurements synchronized with flares, which are still unpredictable events. This paper is a case study of one instance of such synchronization, where cancellation analysis has been performed on AR NOAA10019, confirming the occurrence of topological changes of magnetic structures related to flaring activity.

2. Signed measure and cancellation analysis

Solar active regions are often characterized by scale dependent formation of energetic and localized structures (Abramenko et al. 1998). Structures can be seen as smooth regions of the magnetic field, embedded in a highly fluctuating background. For zero-mean fields, they can be associated to scale dependent, signed fluctuations of the fields. By introducing a signed measure (as opposed to the usual positive defined probability measure), it is possible to characterize the scaling properties of sign oscillations (or sign persistence) of the fields (Ott et al. 1992). Therefore, it is possible to study the presence and the topological characteristics of structures defined in sign. Signed measure has been successfully used to describe photospheric velocity structures (Consolini et al. 1999), and more extensively for the study of current structures in MHD (Sorriso-Valvo et al. 2002; Graham et al. 2005), Hall-MHD (Martin et al. 2013), and Vlasov-Maxwell (De Vita et al. 2014) numerical simulations. Applications to measurements of magnetic vectors in solar active regions have confirmed cancellation analysis as an interesting tool to detect changes in the scaling properties of the fields' fluctuations, and of the fractal

dimension of the associated gradients (Abramenko et al. 1998; Yurchyshyn et al. 2000; Sorriso-Valvo et al. 2004).

The signed measure of a zero-mean scalar field $f(\mathbf{r})$ can be defined on a d-dimensional set $Q(L)$ of size L as follows (Ott et al. 1992). Let $\{Q_i(l) \subset Q(L)\}$ be a partition of $Q(L)$ in disjoint subsets of size l. Then, for each scale l and for each disjoint set of boxes $Q_i(l)$, the signed measure is

$$\mu_i(l) = \frac{\int_{Q_i(l)} \mathrm{d}\mathbf{r}\, f(\mathbf{r})}{\int_{Q(L)} \mathrm{d}\mathbf{r}\, |f(\mathbf{r})|}. \quad (1)$$

When the size of the subset $Q_i(l)$ is large, cancellations between small structures of opposite sign occur within each box, resulting in small contribution to the signed measure. However, as the boxes become smaller and reach the typical size of the structures, each box is more likely to contain a single, sign defined structure, reducing the level of cancellations. The way this happens can be statistically characterized through the "partition function":

$$\chi(l) = \sum_{Q_i(l)} |\mu_i(l)|, \quad (2)$$

where the sum is extended to all disjoint subsets $Q_i(l)$. If the partition function has power-law scaling $\chi(l) \sim l^{-\kappa}$, the measure is sign singular, and κ is referred to as cancellation exponent. The latter represents a quantitative measure of the cancellation processes. For example, a smooth field will have scale independent, little, or no cancellations, resulting in constant partition function ($\kappa = 0$). On the other hand, for statistical reasons, a completely stochastic process with randomly distributed fluctuations over the whole domain will have cancellations proportional to the square root of the volume, so that the partition function will have a cancellation exponent given by $\kappa = d/2$ (Vainshtein et al. 2007). This indicates that cancellation exponents can be used to characterize the scaling properties of the field fluctuations. Furthermore, a simple geometrical argument, based on the separation of the field in correlated (the structures) and uncorrelated (the background field) subsets, establishes a phenomenological relationship between the cancellation exponent and the fractal dimension D of the typical dissipative structures of the flow, so that (Sorriso-Valvo et al. 2002)

$$\kappa = (d - D)/2. \quad (3)$$

It should be pointed out that the use of one single fractal dimension cannot fully capture all the fine details of the typical plasma turbulence processes, which are more likely characterized by multifractal scaling (Muller & Biskamp 2000). Nonetheless, D still represents a useful indicator of the topological characteristics of the "mean" intermittent structures of the flow.

3. THEMIS data: active region NOAA10019

In this paper we provide an example of application and validity of the cancellation analysis for identifying correlations between topological changes of photospheric magnetic field and occurrence of flares. Toward this goal, the technique was applied to a time series of magnetograms in active region NOAA10019. Observations of this active region were performed between July 3 and July 6, 2002 by exploiting the spectro-polarimetric mode of the ground-based THEMIS telescope,[1] using the photospheric Fe I 630.2 nm spectral line (Briand & Vecchio 2003). The observed active region was located around $E39-S17$ on the first day of observation, and reached W08–S17 on the last day. The active region was therefore located close to the solar center, where perspective effects are reduced. The spatial sampling along the slit was 0.5″/pixel (the size of the spectrograph entrance slit's width) and the spectral sampling 22 mÅ/pixel. The size of field covered by the magnetogram varied from 111×143 to 241×143 pixels. The four Stokes parameters I, V, Q, U were measured using an exposure time of 300 ms for all wavelengths. The field of view covered by the entrance slits of the spectrograph was 1′. The so-called $2 \times 1'$ THEMIS spectro-polarimetric configuration was used: the two beams with orthogonal polarization exiting the analyzer were directed into one single camera. Beam inversion was performed for the linear polarization Q: the top part of the camera received sequentially $I + Q$, $I - Q$, $I + U$, and $I - V$, while the bottom part recorded $I - Q$, $I + Q$, $I - U$, $I + V$. This observing strategy allowed to reduce the impact of the seeing-induced cross-talk between Stokes parameters, due to the time delay between two successive polarimetric measurements (1 s) (Skumanich et al. 1997). The final error of the measurements is $S/I_c = 10^{-3}$, where S stands for one of the Q, U, or V Stokes parameters and I_c stands for the intensity of the continuum in quiet Sun regions. To derive the magnetic field strength, inclination, and azimuth, the SIR (Stokes Inversion based on Response function), implemented by choosing a one component atmosphere, was used (Ruiz Cobo & del Toro Iniesta 1992). The 180°-ambiguity of the azimuth ϕ was solved by exploiting the property that the penumbral magnetic field is planar and its azimuth changes with continuity. Therefore, following likelihood arguments, the azimuth was fixed by continuity, starting from areas where it is well defined. Magnetic fields were then expressed in the local reference frame coordinates in which the z component is perpendicular to the solar surface at the point of observation.

In this work, a time series of 15 maps of the vector magnetic field in NOAA10019 was used. The time series starts on July 3 at 08:06 (in Universal Time, UT) and ends on July 6 at 11:39 UT. Dataset for each of the four days includes six, three, two, and four snapshots of the active region, respectively. Due to the absence of an image stabilization system, the THEMIS magnetograms of the target region of the slit were subject to image distortion, caused by the seeing variations. This typically produces artificial image shifting along the slit that results in a stripped pattern on the images. The typical size of such pattern is the slit width, i.e. one pixel in the magnetograms. This could affect the calculation of the current density. In order to correct for this distortion, we used a 1D non-linear filter on each row of the magnetograms (i.e. transverse with espect to the slit direction). The filter is conceived to locally identify and eliminate (through interpolation) the field fluctuations of a given width (Naudy & Dreyer 1968). We have checked that the filter width of one pixel was enough to remove from the magnetograms the stripped pattern due to seeing. Figure 1 shows an example of comparison between the original (a) and filtered, (b) data. As can be seen, the vertical stripes observed in the original data are removed in the filtered magnetograms. Figure 2 shows four examples of the active region field of view, namely the intensity image at Fe I 630.2 nm line center, on four different days of observation.

[1] http://www.themis.iac.es

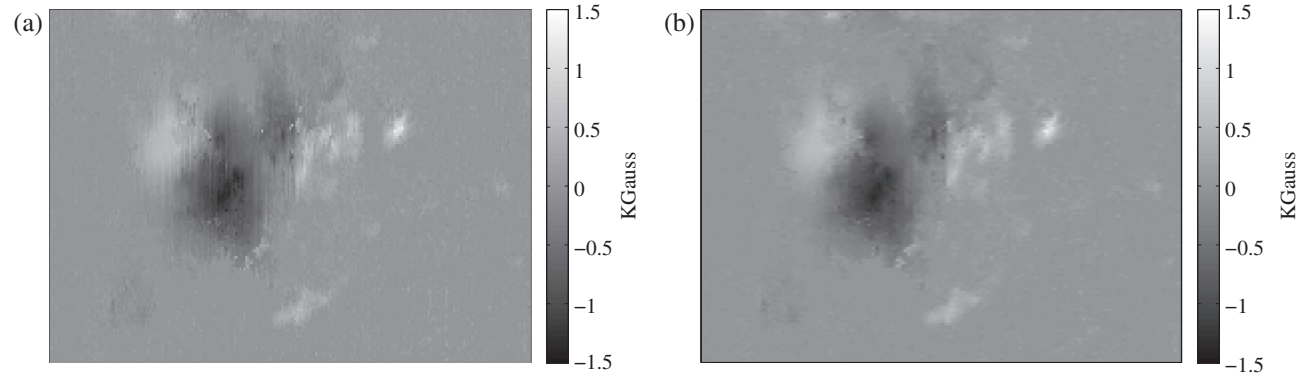

Fig. 1. An example of application of the non-linear filter described in the text. Left panel (a): one snapshot of the magnetic field component B_x of the time series. The vertical stripped pattern due to seeing conditions is clearly visible. Right panel (b): the same field after application of the non-linear filter for one pixel width anomalies (Naudy & Dreyer 1968). The vertical stripes observed in the original data are effectively removed.

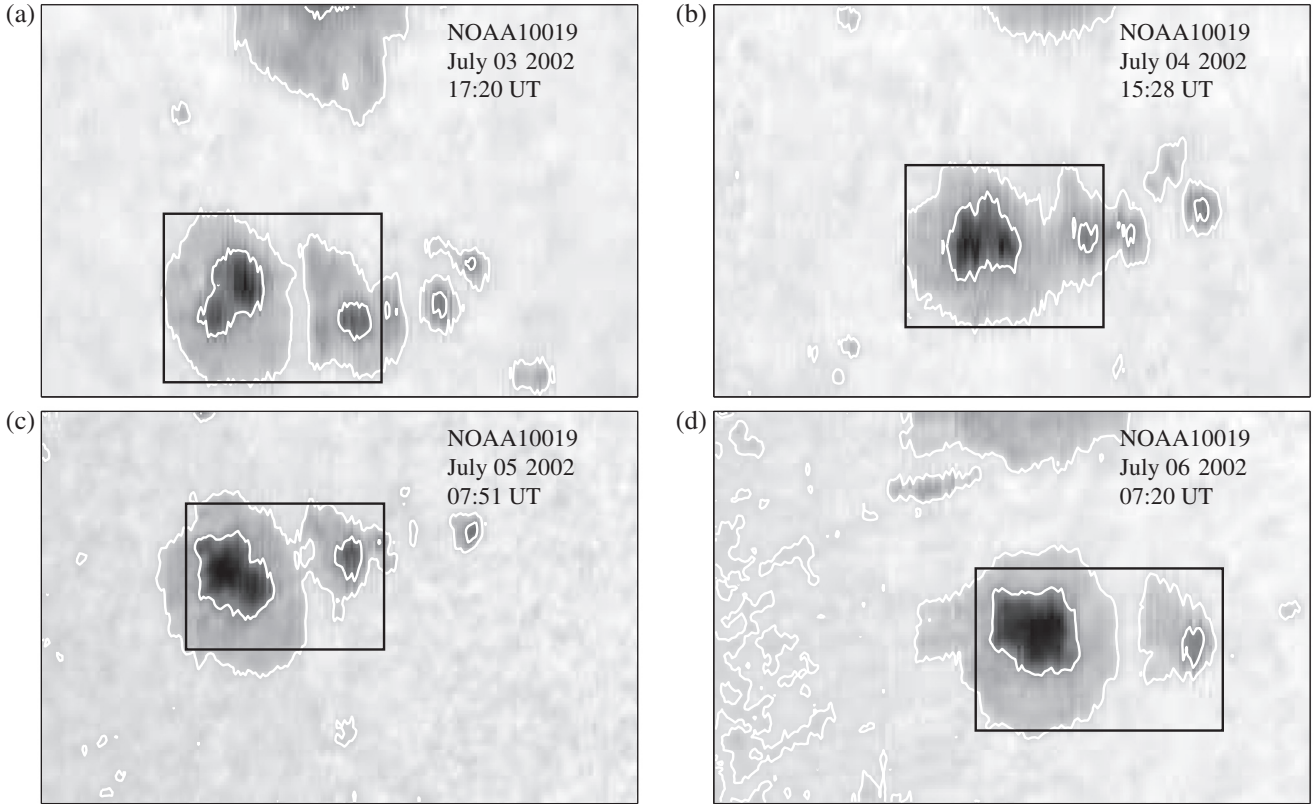

Fig. 2. Field of view of the AR NOAA10019 as measured on July 3 (a), 4 (b), 5 (c), and 6 (d), 2002 (intensity image at Fe I 630.2 nm line center). The time of each snapshot is indicated in the legend. Boxes indicate the portion of image used for the analysis.

The sunspot umbral and penumbral boundaries are marked by the contour lines of the Fe I, set at about 90% and at 70% of the quiet sun intensity, respectively. In the legend of Figure 2, the day, hour (in Universal Time) are indicated, along with a letter identifying the snapshot. The boxes $Q(L_x, L_y)$ of dimensions $L_x \simeq 80$ and $L_y \simeq 50$ pixels (corresponding approximately to 30×20 Mm) used for the estimation of the cancellation exponents (see Sect. 4 for the description) are shown for each snapshot (black lines). In Figures 3–5, we display four snapshots of the maps of each of the three filtered magnetic field components B_x, B_y, and B_z, for the AR NOAA10019. Again, each snapshot refers to a different day of the observation, as indicated in the legend of Figure 2. Finally, using the two-dimensional measurements of the photospheric vector magnetic field $\mathbf{B}(x, y)$ on the solar surface, it was possible to estimate the vertical component z of the current density $J_z(x, y) = (c/4\pi)(\nabla \times \mathbf{B})_z$, where (x, y) are the Cartesian coordinates on the surface of the Sun. This was done by computing, for each pixel of area s, the line integral of the vertical component of the magnetic field $B_z(x, y)$ over a closed contour G (Yurchyshyn et al. 2000), $4\pi J_z/c = (\nabla \times \mathbf{B})_z = s^{-1} \oint_G \mathbf{B}_\perp \cdot d\mathbf{r}$. Integration along each side of G was performed using Simpson's rule. Figure 6 shows the vertical current density J_z for the same snapshots as in Figure 2.

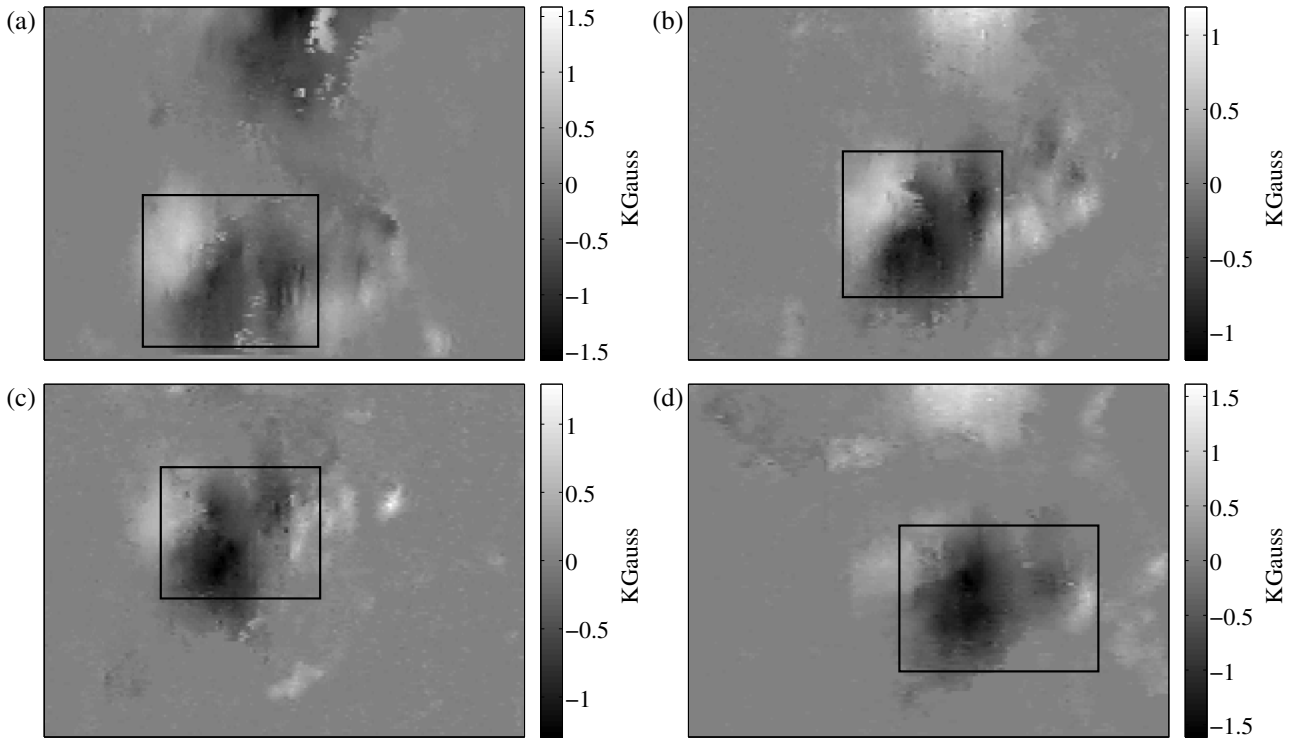

Fig. 3. Maps of filtered horizontal magnetic field component B_x for the AR NOAA10019 as measured on July 3 (a), 4 (b), 5 (c), and 6 (d), 2002. Time of each snapshot is indicated in the legend of Figure 2. For each snapshot, boxes indicate the portion of image used for the analysis.

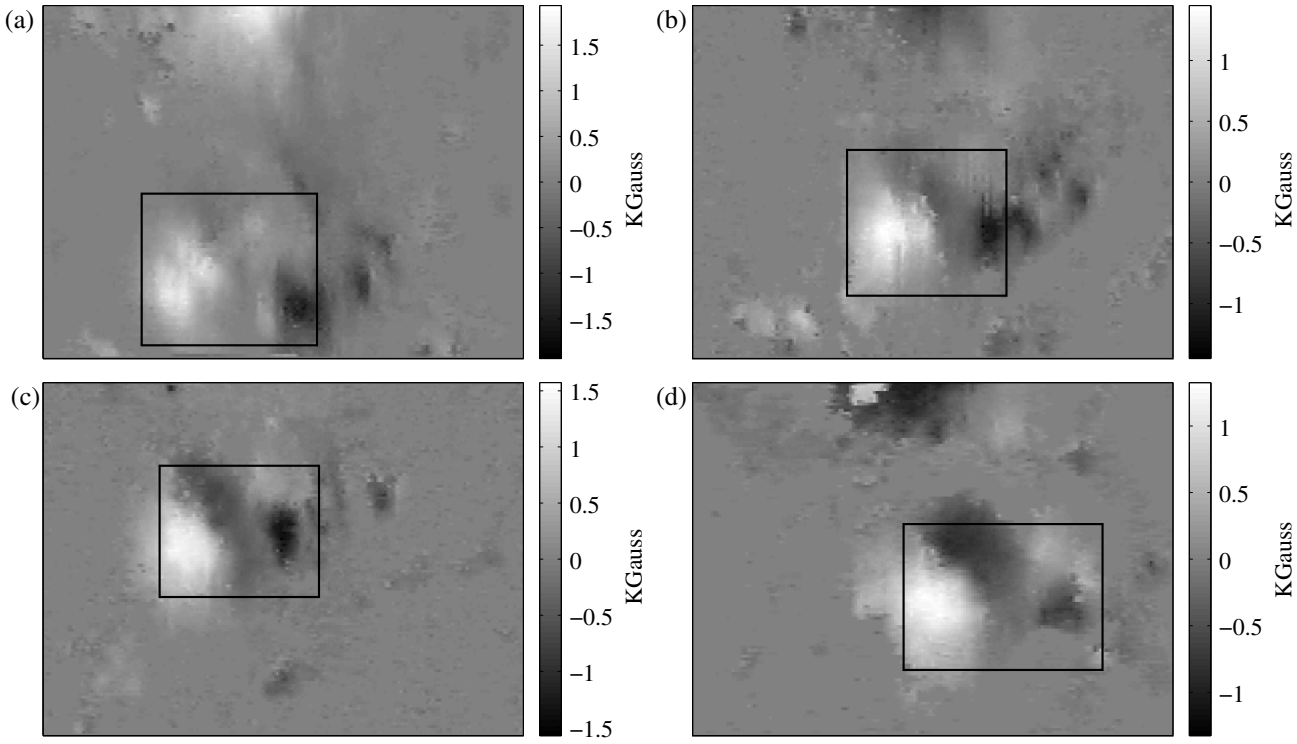

Fig. 4. Maps of filtered horizontal magnetic field B_y for the AR NOAA10019 as measured on July 3 (a), 4 (b), 5 (c), and 6 (d), 2002. Time of each snapshot is indicated in the legend of Figure 2. For each snapshot, boxes indicate the portion of image used for the analysis.

4. Cancellation analysis of the current density

Once the vertical current density has been calculated, cancellation analysis was performed for each filtered snapshot of the time series. In order to mitigate noise, portions of the images with low current were eliminated by using reduced boxes $Q(L_x, L_y)$ of minor size varying from $L_y = 50$ to $L_y = 70$ pixels, which track the central part of the active region. Examples of these boxes are depicted in Figures 2–6. Additionally, in order to get a statistically more robust estimate of the cancellation

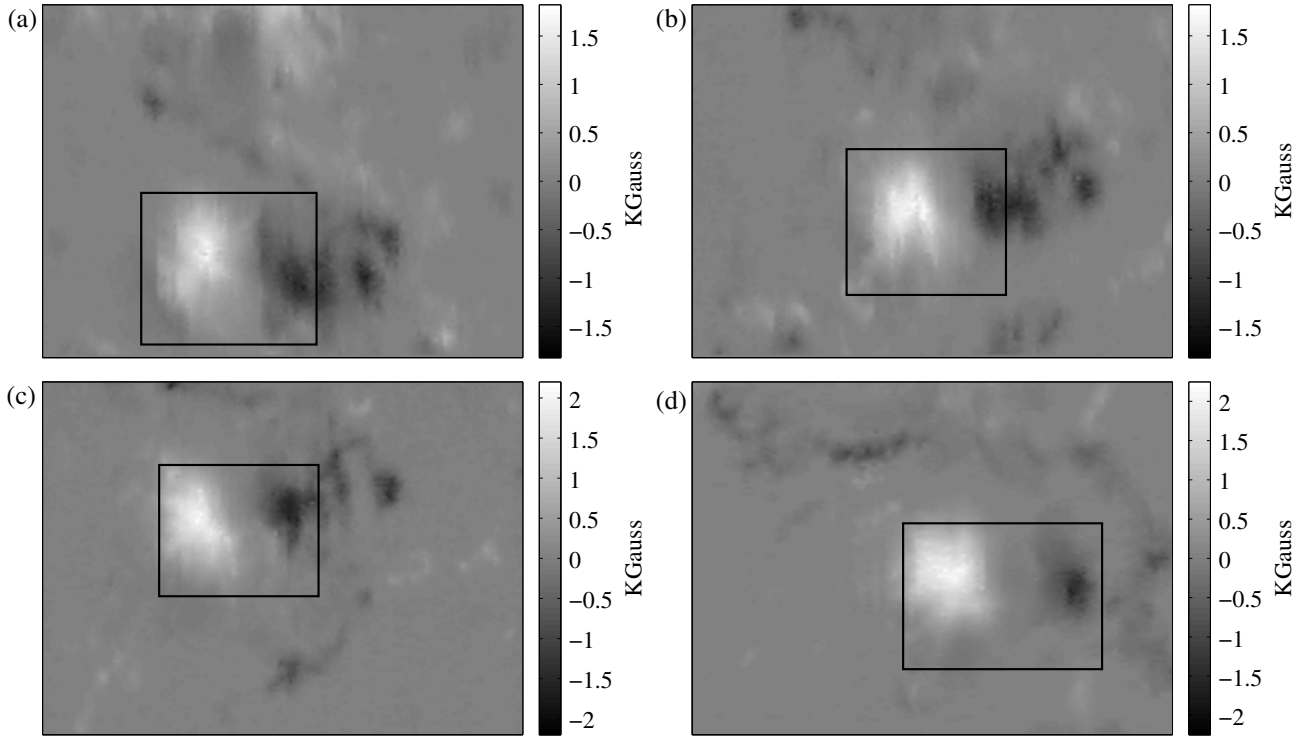

Fig. 5. Maps of filtered vertical magnetic field B_z for the AR NOAA10019 as measured on July 3 (a), 4 (b), 5 (c), and 6 (d), 2002. Time of each snapshot is indicated in the legend of Figure 2. For each snapshot, boxes indicate the portion of image used for the analysis.

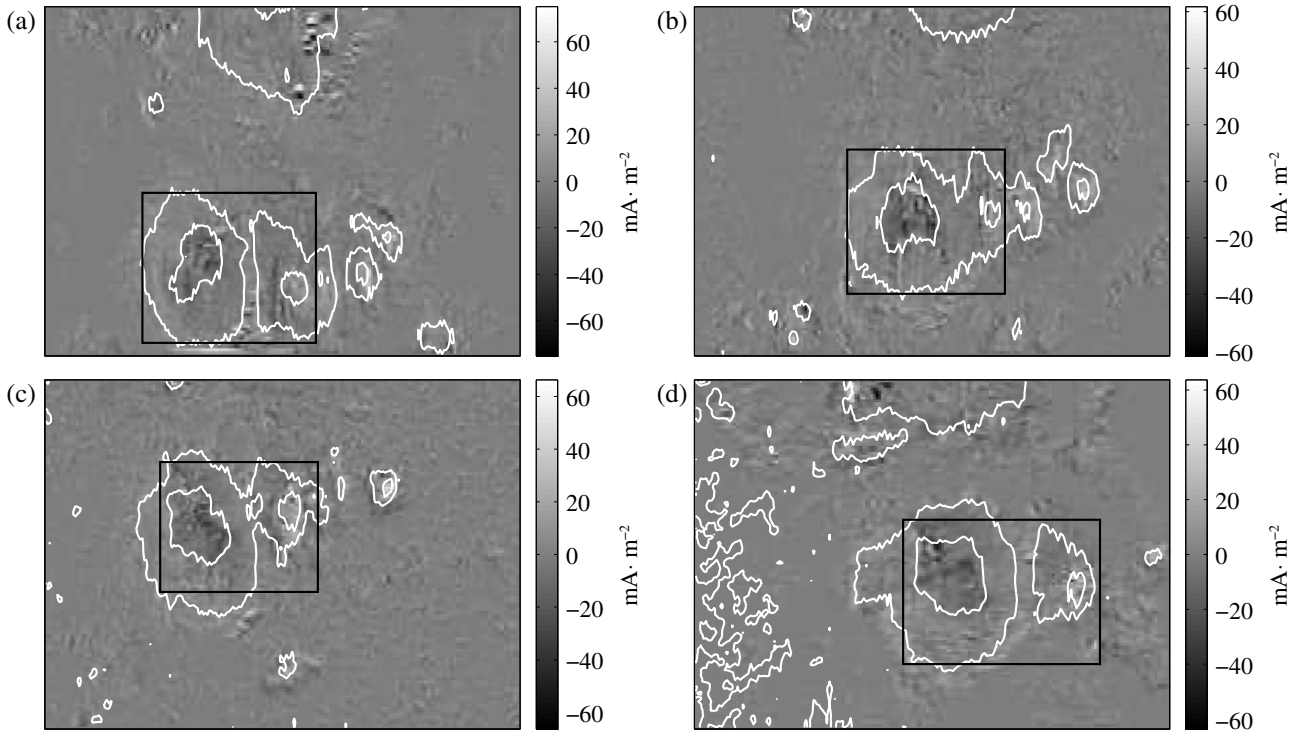

Fig. 6. Maps of vertical component of the current density J_z for the AR NOAA10019 as measured on July 3 (a), 4 (b), 5 (c), and 6 (d), 2002, as indicated in Figure 2. The sunspot umbral and penumbral boundaries are marked by the contour lines of the visible light intensity (white line). For each snapshot, boxes indicate the portion of image used for the analysis.

exponents, the partition functions were computed using slightly smaller boxes $Q(L)$, with $L \simeq 50$ pixels ($\simeq$20 Mm) spanning the whole domain $Q(L_x, L_y)$ by recursively shifting by steps of three pixels in one or both directions in the $(x - y)$ plane. This provided, for each snapshot, N subsamples (N varying from 18 to 24, depending on each snapshot's size). The signed

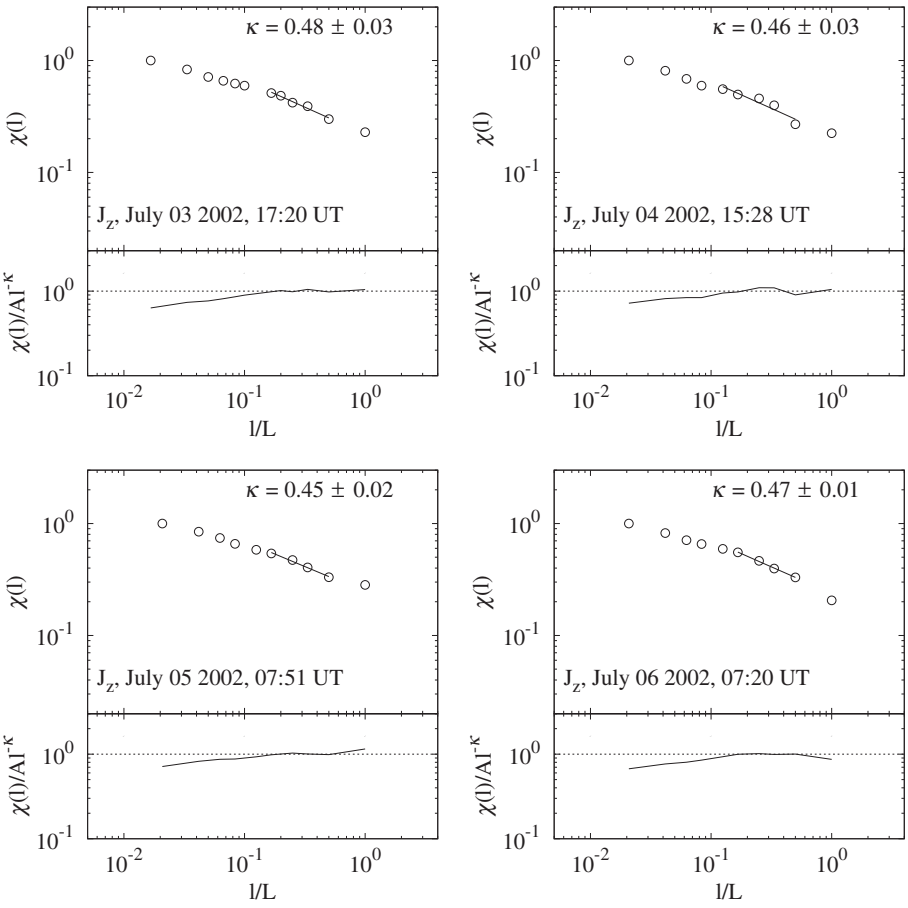

Fig. 7. The averaged partition functions for the four snapshots shown in Figure 6. A power-law fit $\chi(l) = A(l/L)^{-\kappa}$ is superimposed on each partition function. In the bottom section of each panel, the partition function is compensated by multiplying for the fitted power law, so that the actual power-law range is visible as horizontal line.

measure was then estimated for each of the N sub-sample $Q(L)$ as

$$\mu_i(l) = \frac{\int_{Q_i(l)} J_z(x,y)\mathrm{d}x\mathrm{d}y}{\int_{Q(L)} |J_z(x,y)|\mathrm{d}x\mathrm{d}y}. \quad (4)$$

For each snapshot and for each scale, the average and standard deviation of the N "running" partition functions were then evaluated. The averaged partition functions were finally used for the analysis, and the standard deviation was used as the corresponding uncertainty (Yurchyshyn et al. 2000). Since the power-law fitting range is limited, the robustness of the cancellation exponent was further tested by allowing the fitting range to shift, expand, or reduce by one or two points in the partition function. The range spanned by the resulting fitting parameter also provides a possible uncertainty on the estimate of the cancellation exponent.

Examples of the partition functions, as obtained from the four photospheric current density snapshots shown in Figure 6, are plotted in Figure 7, together with a power-law fit $\chi(l) = A(l/L)^{-\kappa}$, performed in the range where there is suggestion of power-law behavior. The latter provides the values of the cancellation exponents κ (indicated in each panel). The bottom frame of each panel of Figure 7 shows the partition functions compensated dividing by the fitted power law, so that a power-law range appears as constant. The cancellation exponents found for the time series were relatively stable, so that the average value is $\langle\kappa\rangle = 0.43 \pm 0.01$, the uncertainty being the standard deviation. The remarkable deviation from the value $\kappa = 1$, typical of stochastic fluctuation, indicates the presence of strongly sign persistent current structures in the AR. Note that the filter technique used to remove the seeing does not sensibly affect the power-law fit, because it only acts at small scales (of the order of 1 Mm), far from the actual fitting range (the smallest fitted scale being of about 3.5 Mm). We point out that the analysis of the vertical photospheric magnetic field $B_z(x, y)$ (not shown) has provided negligible cancellation exponents, of the order of 10^{-2}, indicating that the measured magnetic field is composed of large unipolar structures. This was already observed in former analysis (Lawrence et al. 1993; Abramenko et al. 2000).

5. Time evolution and flaring activity

X-ray observation of the active region NOAA10019 showed periods of low and enhanced flaring activity. During the observations, the active region produced eight C-class flares whose list, as extracted from GOES X-ray flux database, is given in Table 1. Figure 8 shows the peak X-ray flux for the flares listed in the table (vertical bars, right y-axis), measured in active region NOAA10019 during the time of observation. The time axis is set so that $t = 0$ at 00:00 UT on July 3, 2002, the first day of observation. In the same plot, we display the time evolution of the fractal dimension of current structures D (symbols

Table 1. Row 1: the start time of flares occurring since 00:00 UT on 3 July 2002 and for the whole observation period. Row 2: the class of flares (full disk emission from GOES X-ray database).

t(h)	7.95	8.80	11.72	28.58	40.35	41.68	63.83	81.45
Class	C3.4	C1.1	C7.3	C4.5	C3.4	C2.4	C6.3	C6.0

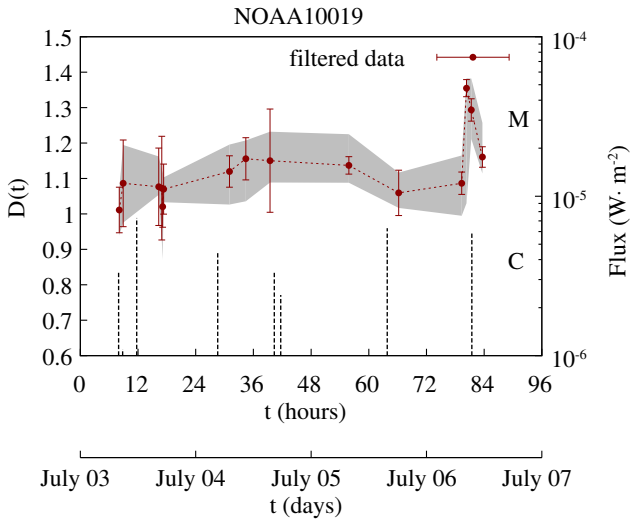

Fig. 8. Fractal dimension of the photosperic current density structures D versus time (symbols connected by solid line, left vertical axis). The vertical lines show the X-ray class of flares (right y-axis). The gray area indicates the range of variability due to modification of the fitting range.

and dashed line, left y-axis), as calculated from the fitting parameter κ through the relation (3). The error bars are the standard deviation of the exponents over the different sub-sets of each snapshot, while the gray shaded area is the error associated with the choice of the fitting range, i.e. the range of variation of the cancellation exponent due to any reasonable shift of fitting range. During the first part of the observation, the fractal dimension remained roughly steady, with $D \simeq 1$, which is the value expected in the presence of one-dimensional current filaments. However, a sudden increase from $D(t_1) = 1.10$ to about $D(t_2) = 1.38$ is clearly present near the end of the observation, between $t_1 = 79.33$ h, or 07:20 UT, and $t_2 = 80.33$ h, or 08:20 UT, both on July 6. This increase occurs corresponding to a C-class flare (with flux above 10^{-6} W/m^2) recorded at $t_F = 81.45$ h or 09:27 UT on the same day. This observation, similar to previous results (Abramenko et al. 1998; Yurchyshyn et al. 2000; Sorriso-Valvo et al. 2004), suggests that the magnetic field structures could be smoothed out by dissipative effects which anticipate the flare explosion.

The sharp jump observed in the fractal dimension was $\Delta D_{12} = |D(t_2) - D(t_1)| = 0.28$. This value represents a significant 25% variation relative to the mean dimension $\langle D \rangle = 1.13$, and a nontrivial factor 10 in units of standard deviation $\sigma_D = 0.03$. Both the average and the standard deviation were computed over the whole observation time. Furthermore, the jump is also significant with respect to the possible error deriving from the shift of the fitting range, evidenced in gray. This is also clear from the direct observation of the two partition functions, reproduced in bottom panel of Figure 9 for the two snapshots at t_1 and t_2. The corresponding current maps are reported in the top panels of the same figure.

In order to test for reliability of the observed change of fractal dimension and for the validity of the non-linear filter, we compared the filtered data with the original data. Furthermore, we tested the robustness of the results with respect to stronger seeing image degradation by artificially reducing the data resolution. To evaluate the effect of image distortion on the slope of the sign-singularity spectrum, all components of each magnetic field vector, within each original magnetogram, have been smoothed over 3×3 or 5×5 pixels, before recalculating the current density and performing the cancellation analysis (Yurchyshyn et al. 2000). In Figure 10 we show one example of the scaling behavior of the partition function $\chi(l)$ for the four cases, namely: the original data (circles), the filtered data (squares), the 3×3 pixels smoothed data (diamonds), and the 5×5 pixels smoothed data (triangles). The example shown here refers to the snapshot taken at 17:20 UT on July 3, 2002. For the smoothed fields, the small scale saturation of the partition functions was observed to cover an increasingly large range of scales, as the smoothing area increases. This is a trivial consequence of the field becoming smoother, so that sign singularities are no longer present (Yurchyshyn et al. 2000). Note that the partition function of the unsmoothed field does not saturate to unity, probably because elementary flux tube is smaller than the instrumental resolution (Sorriso-Valvo et al. 2002). Compared to the original data case, in the intermediate region of scales the cancellation exponent is found to slightly decrease with the size of the smoothing area, as indicated in the legend. The non-linear filtered data also show a decrease in the dimension. However, the relative variation of the scaling exponent in these cases is always less than 10%. Figure 11 shows the time dependence of dimensions D for the four series. While the general effect of the filtering and smoothing was the evident increase in fractal dimension, the main features of the time dependence, and in particular the sharp jump observed on the last day, were not lost, resulting in a robust 25% increase of D in all cases. More quantitatively, the mean increase of the dimension ΔD_x due to the filtering (subscript x = filter) and to the $n \times n$ smoothing (subscript $x = Sn$ with $n = 3, 5$) was evaluated. This was done by averaging the differences $|D_x - D_{\text{original}}|$ over the whole time window, obtaining $\Delta D_{\text{filter}} = 0.04$, $\Delta D_{S3} = 0.04$, and $\Delta D_{S5} = 0.09$. Therefore, the observed jump is always significantly larger than the filtering and smoothing effect, $\Delta D_{12} > \Delta D_x$, confirming the goodness of the observation.

Therefore, since the cancellation exponent is robust with respect to the filter or degree of smoothing, we can conclude that the variation of fractal dimension observed for the flare on July 6, 2002 is nontrivial, and does not significantly depend on the measurement resolution.

Incidentally, it is worth noticing that a few similar flares have occurred during the time span of our observation. However, no clear changes in the cancellation exponent were

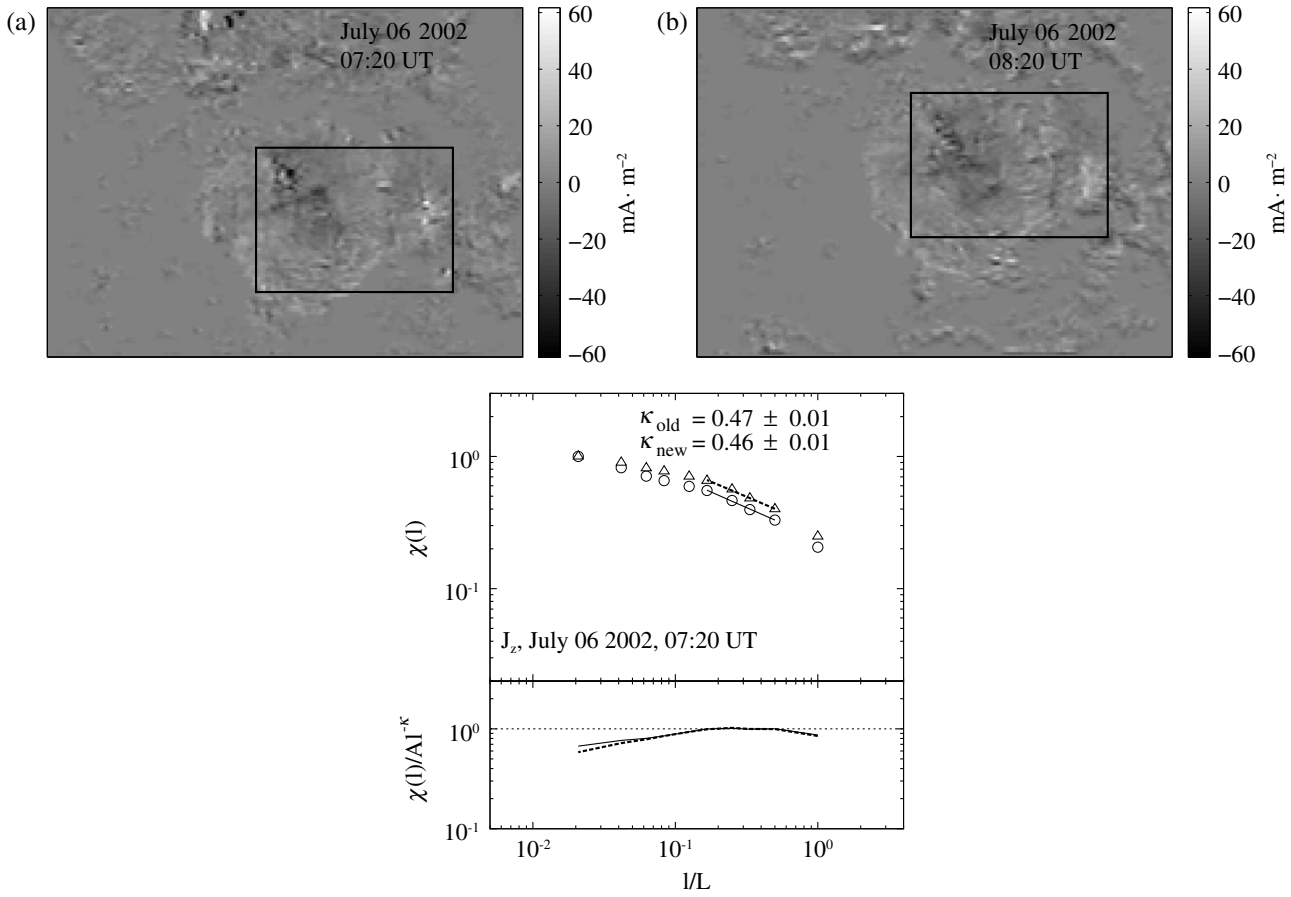

Fig. 9. Top panels: the vertical current J_z before ($t = t_1$ and after ($t = t_2$) the sudden fractal dimension increase. Bottom panel: the partition functions of the above maps, with the power-law fits and the corresponding cancellation exponents.

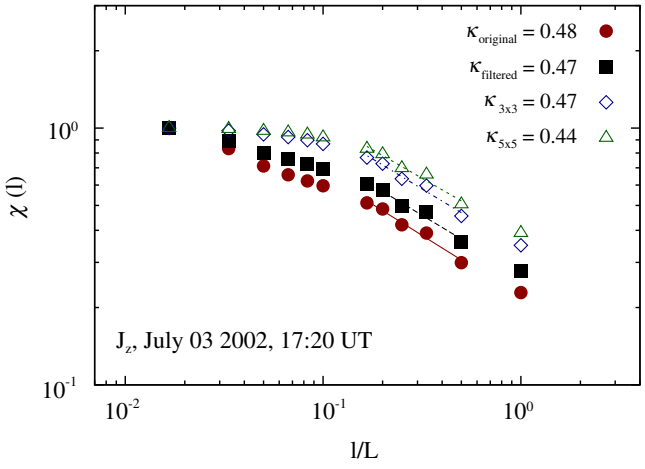

Fig. 10. The partition functions $\chi(l)$ versus the scale (l/L) for the current density J_z calculated for the original data (circles), for the filtered data (squares), and for the smoothed (3 × 3, diamonds, and 5 × 5, triangles) data. This example refers to the snapshot taken on July 3, 2002 at 17:20 UT. Note that the first point at the smallest scale is identically 1 because of the normalization. Cancellation exponents κ obtained through the power-law fit for the four cases are indicated in the legend. The error bar is ±0.03 for all cases.

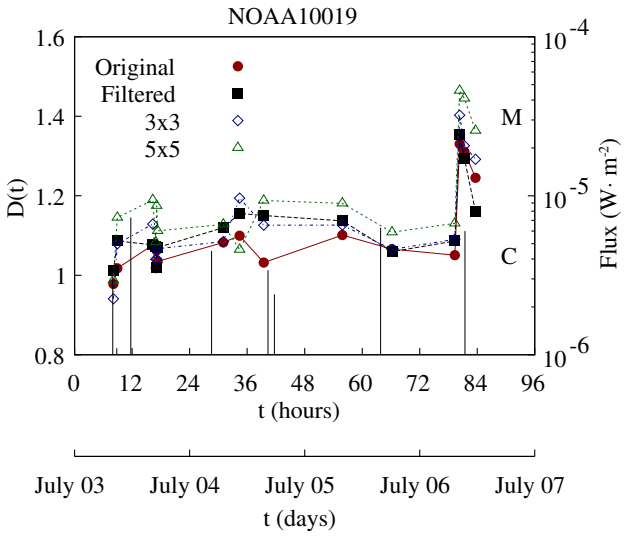

Fig. 11. Fractal dimension versus time for the four datasets, obtained using the original, filtered, and smoothed data (see legend). The vertical lines show the X-ray class of flares (right y-axis).

present in these cases. While this can probably be attributed to the poor temporal sampling of the magnetograms, there is at least one case (the C-class flare around $t = 64$ h) for which the cancellation exponent was estimated only a few hours after the flare, and for which no particular deviation from the mean value is observed. However, with the data at hand it is not possible to assess whether this was due to sampling time

limitations or to a different behavior of the sign-singularity properties.

6. Conclusions

In this paper we used the cancellation analysis technique to investigate the topological properties of the typical current structures in the solar active region NOAA10019. To this purpose, we calculated the vertical component of the current density from magnetic field data acquired by the spectro-polarimetric mode of the ground-based THEMIS telescope, using the photospheric Fe I 630.2 nm spectral line. In particular, we focused on the temporal evolution of the current structures in response to photospheric magnetic field dynamics by studying the variation of the scaling index describing the cancellations of positive and negative current density, which can be related to the typical fractal dimension of the current patterns. In the considered active region, and far from large flares, the values of the cancellation exponent are consistent with the presence of sign-persistent current structures. Moreover, we found that the dynamics of the magnetic field fluctuations and mean vertical current describes quite well the transition of the AR into the flare activity stage. Indeed, during the first days, the fractal dimension showed almost constant values around $D = 1$, compatible with presence of one-dimensional current filaments. On the other hand, with the occurrence of a C-class flare a sudden significant increase, of about 25% relative to the mean fractal dimension, is observed indicating that the current structures are affected by the dissipative effects at work before the flare. The abrupt variation of the fractal dimension is plausibly the signature of dissipation due to reconnection events, which are believed to originate flares. We verified that our results are stable with respect to the application of a nonlinear filter, used to remove the seeing effects from the images. Moreover, robustness of the results was tested by adding an artificial reduction of the spatial resolution, which mimics a stronger seeing-induced image degradation of the magnetic field components. The stability of our results is related to the fact that the spatial scales affected by the seeing, of the order of 1 Mm, are far from the typical size of the current structures, as identified by the bottom of the fitting range (around 3.5 Mm). For both tests, a general increase in fractal dimension is observed, with relative variation below 10%. This value is well below the sharp 25% jump observed at the C-class flare, indicating that the variation of fractal dimension is nontrivial, and does not significantly depend on the measurement resolution and data quality.

The high-quality, space-based data available today (thanks to e.g. Solar Dynamics Observatory [SDO] or Hinode instrumentation) allow the study of extremely fine details of the magnetic complexity, which can help understand better the physical processes occurring in flaring active regions Yurchyshyn et al. (2012), Sorriso-Valvo et al. (2015). Nevertheless, the results presented in this paper, corroborated by the robustness tests, are particularly interesting precisely because the analyzed data are not of high quality, in this case due to seeing conditions and to the lack of compensating technique at the time of the measurements. Indeed, the robustness of the cancellation analysis, even when low quality data are used, suggests that this kind of approach can be used for the analysis of older dataset. This will allow to enrich the statistics of the flare-related topological changes, fundamental for the application of this technique for the purpose of space weather monitoring.

Acknowledgements. The research leading to these results has received funding from the European Community's Seventh Framework Programme FP7-PEOPLE-2010-IRSES under Grant Agreement No. 269297/"TURBOPLASMAS" (http://www.fis.unical.it/astroplasmi/turboplasmas). The authors acknowledge financial support from POR Calabria FSE 2007/2013. The editor thanks two anonymous referees for their assistance in evaluating this paper.

References

Abramenko, V.I., V.B. Yurchyshyn, and V. Carbone. Sign-singularity of the current helicity in solar active regions. *Solar Phys.*, **178**, 35, 1998.

Abramenko, V.I., V.B. Yurchyshyn, and V. Carbone. Flare-related changes of an active region magnetic field. *Astrophys. J.*, **538**, 968, 2000.

Briand, C., and A. Vecchio. Chromospheric polarity reversal on sunspots: new insight from spectro-polarimetric measurements. *A&A*, **403**, L33, 2003, DOI: 10.1051/0004-6361:20030553.

Consolini, G., V. Carbone, F. Berrilli, R. Bruno, B. Bavassano, et al. Scaling behavior of the vertical velocity field in the solar photosphere. *A&A*, **344**, L33, 1999.

De Vita, G., L. Sorriso-Valvo, F. Valentini, S. Servidio, S. Servidio, L. Primavera, V. Carbone, and P. Veltri. Analysis of cancellation exponents in two-dimensional Vlasov turbulence. *Phys. Plasmas*, **21**, 072315, 2014.

Graham, J., P.D. Mininni, and A. Pouquet. Cancellation exponent and multifractal structure in two-dimensional magnetohydrodynamics: direct numerical simulations and Lagrangian averaged modeling. *Phys. Rev. E*, **72**, 045301(R), 2005.

Lawrence, J.K., A.A. Ruzmaikin, and A.C. Cadavid. Multifractal measure of the solar magnetic field. *Astrophys. J.*, **417**, 805, 1993.

Martin, L.N., G. De Vita, L. Sorriso-Valvo, P. Dmitruk, G. Nigro, L. Primavera, and V. Carbone. Cancellation properties in Hall magnetohydrodynamics with a strong guide magnetic field. *Phys. Rev. E*, **88**, 063107, 2013.

Muller, W.C., and D. Biskamp. Scaling properties of three-dimensional magnetohydrodynamic turbulence. *Phys. Rev. Lett.*, **84**, 475, 2000, DOI: 10.1103/PhysRevLett.84.475.

Naudy, H., and H. Dreyer. Essai de filtrage nonlineare applique aux profils aeromagnetiques. *Geophysical Prospecting*, **16**, 171, 1968.

Ott, E., Y. Du, K.R. Sreenivasan, A. Juneja, and A.K. Suri. Sign-singular measures: fast magnetic dynamos, and high-Reynolds-number fluid turbulence. *Phys. Rev. Lett.*, **69**, 2654, 1992.

Ruiz Cobo, B., and J.C. del Toro Iniesta. Inversion of Stokes profiles. *Astrophys. J.*, **398**, 375, 1992, DOI: 10.1086/171862.

Skumanich, A., B.W. Lites, V. Martinez Pillet, and P. Seagraves. The calibration of the advanced stokes polarimeter. *Astrophys. J. Suppl.*, **110**, 357, 1997.

Sorriso-Valvo, L., V. Carbone, A. Noullez, H. Politano, A. Pouquet, and P. Veltri. Analysis of cancellation in two-dimensional magnetohydrodynamic turbulence. *Phys. Plasmas*, **9**, 89, 2002.

Sorriso-Valvo, L., V. Carbone, P. Veltri, V.I. Abramenko, A. Noullez, H. Politano, A. Pouquet, and V.B. Yurchyshyn. Topological changes of the photospheric magnetic field inside active regions: a prelude to flares? *Planet. Space Sci.*, **52**, 937, 2004.

Sorriso-Valvo, L., G. De Vita, M. Kazachenko, S. Krucker, L. Primavera, et al. Sign singularity and flares in solar active region NOAA 11158. *Astrophys. J.*, **801**, 36, 2015, DOI: 10.1088/0004-637X/801/1/36.

Vainshtein, S.I., Y. Du, and K.R. Sreenivasan. Sign-singular measure and its association with turbulent scalings. *Phys. Rev. E*, **49**, R2521, 2007.

Yurchyshyn, V.B., V.I. Abramenko, and V. Carbone. Flare related changes of an active region magnetic field. *Astrophys. J.*, **538**, 968, 2000.

Yurchyshyn, V., V. Abramenko, and H. Watanabe, Hinode-3: The 3rd Hinode Science Meeting, Proceedings of the conference held 1–4 December 2009 at Hitotsubashi Memorial Hall, Tokyo, Japan. In: T. Sekii, T. Watanabe, and T. Sakurai, Editors. ASP Conference Series, Vol. 454, Astronomical Society of the Pacific, San Francisco, 2012, p. 311.

Cite this article as: De Vita G, Vecchio A, Sorriso-Valvo L, Briand C, Primavera L, et al. Cancellation analysis of current density in solar active region NOAA10019. *J. Space Weather Space Clim.*, **5**, A28, 2015, DOI: 10.1051/swsc/2015029.